ARCHIVES OF ELECTRICAL ENGINEERING VOL. 69(2), pp. 303–317 (2020)

DOI 10.24425/aee.2020.133027

Performance analysis and comparison of PMSM with concentrated winding and distributed winding

HONGBO QIU, YONG ZHANG, CUNXIANG YANG, RAN YI

School of Electrical and Information Engineering
Zhengzhou University of Light Industry
No. 5 Dongfeng Road, Zhengzhou, Henan province, China, 450002
e-mail: zhangxiaoyong10056@163.com

(Received: 01.08.2019, revised: 15.11.2019)

Abstract: The concentrated winding (CW) is obviously different from the traditional distributed winding (DW) in the arrangement of windings and the calculation of winding factors, which will inevitably lead to different performances of the permanent magnet synchronous motor (PMSM). In order to analyze the differences between the CW and the DW in the performance, a 3 kW, 1500 r/min PMSM is taken as an example to establish a 2-D finite element model. The correctness of the model is verified by comparing experimental data and calculated data. Firstly, the finite element method (FEM) is used to calculate the electromagnetic field of the PMSM, and the performance parameters of the PMSM are obtained. On this basis, the influences of the two winding structures on the performance are quantitatively analyzed, and the differences between the two winding structures on the performance of the PMSM will be determined. Finally, the differences of efficiency between the two winding structures are obtained. In addition, the influences of the winding structures on eddy current loss are further studied, and the mechanism of eddy current loss is revealed by studying the eddy current density. The analysis of this paper provides reference and practical value for the optimization design of the PMSM.

Key words: air-gap flux density, cogging torque, concentrated winding, distributed winding, efficiency, loss, PMSM

1. Introduction

The PMSM is widely used in electronic information, electric vehicles, wind power generation, aerospace, intelligent robots and other fields because of its advantages of simple structure, high efficiency and a high power factor [1, 2]. The winding of the PMSM is the key component of its energy conversion. The reasonable design of the winding is directly related to the overall performance of the PMSM. The unreasonable design of the windings may cause a series of problems, such as asymmetric motor windings, low winding factors and high harmonic content, which will lead to increased loss, permanent magnet demagnetization and degaussing at a high temperature, electromagnetic vibration and torque ripple. The above reasons put forward higher requirements for the design of motor windings. Therefore, it is of great significance to compare and analyze the performance difference between the centralized winding (CW) and distributed winding (DW).

In recent years, many scholars have made relevant studies on the winding design. In reference [3], based on the PMSM with distributed and concentrated windings, for an x-by-wire application different pole numbers and winding configurations are investigated for the lowest torque pulsation at fault-condition. In references [4] and [5], the induction machine performance with fractional-slot concentrated windings was assessed using the standard distributed lap windings as reference. The different designs are compared and various performance trade-offs highlighted. In reference [6], the effects that fractional-slot concentrated windings have on the d-axis and q-axis inductances of the IPM machine, in comparison with an integral-slot distributed winding, are studied. Reference [7], this paper examines the relationship between rotor design, saliency-based signal injection sensorless control, and power conversion properties for four industrially relevant interior permanent-magnet machine configurations. However, many scholars have not comprehensively analyzed the difference between the two winding structures, and the mechanism of the distinction has not been revealed.

In this paper, a 3 kW 1500 r/min PMSM is taken as an example and based on the FEM. The no-load back EMF, air-gap flux density, torque ripple, cogging torque as well as loss of the CW and the DW are compared and analyzed. The distinctions of the above performances are obtained and the reasons for the distinctions are analyzed theoretically. In addition, the mechanism of eddy current loss is revealed by studying the eddy current density and the total harmonic distortion (THD) of air-gap flux density at rated operation. Some useful conclusions are obtained, which could provide the basis for the further research on the PMSM.

2. Motor parameters and models

2.1. Finite element models

In order to analyze the distinctions between the CW and DW in performance, a 3 kW, 1500 r/min PMSM is taken as an example. According to the structures and parameters of the prototype, the finite element models of different winding structures are established. In order to more accurately compare the difference between the DW and the CW, we ensure that two types of motors operate at the same power or at the same voltage level. In order to ensure the accuracy of the analysis results, some parameters of the two motors are guaranteed to be the same when the model is established, as shown in Table 1. Fig. 1 shows the finite element model of the PMSM with the CW and DW.

In the PMSM electromagnetic analysis process, in order to simplify the calculation, the following assumptions are made [8]:

1. Displacement currents and skin effect in the stator windings are ignored.

Table 1. Basic parameters of prototype

Parameters	**Value**	
	12slot-CW	**30slot-DW**
Rated speed (r/min)	1500	
Rotor magnetic circuit structure	Surface-mounted type	
Stator outer diameter (mm)	172	
Stator inner diameter (mm)	101	
Rotor outer diameter (mm)	99	
Rotor inner diameter (mm)	30	
Axial length of stator core (mm)	62	
Number of parallel branches	2	
Winding connection type	Y	
Air gap length (mm)	1	
Number of poles/slots	10/12	10/30

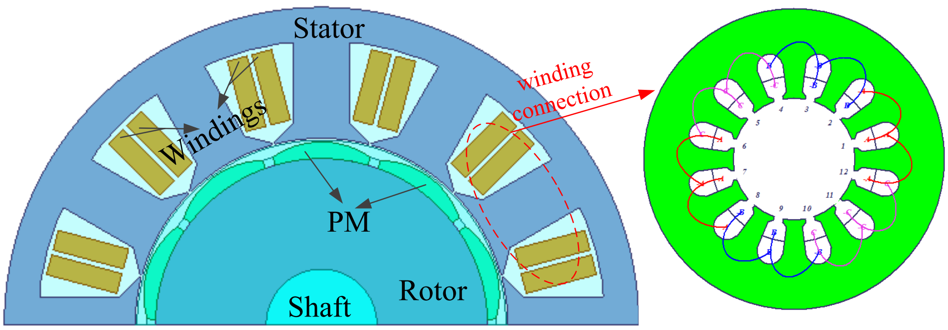

(a) The finite element model of CW-12slot

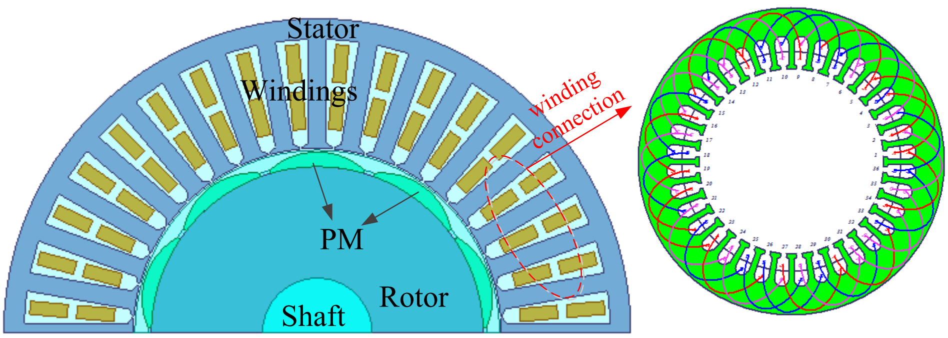

(b) The finite element model of DW-30slot

Fig. 1. Finite element model of prototype

2. Ignoring the influence of the PMSM displacement current, the parallel plane field perpendicular to the motor shaft is adopted to analyze the electromagnetic field of the PMSM.
3. The influences of the PMSM temperature on material conductivity and magnetic conductivity are ignored.

The calculation formula of a two-dimensional electromagnetic field is shown in (1) [9]:

$$\begin{cases} \Omega: & \dfrac{\partial}{\partial x}\left(\dfrac{1}{\mu}\dfrac{\partial A_z}{\partial x}\right) + \dfrac{\partial}{\partial y}\left(\dfrac{1}{\mu}\dfrac{\partial A_z}{\partial y}\right) = -J_z + \sigma\dfrac{\mathrm{d}A_z}{\mathrm{d}t} \\ \Gamma_1: & A_z = 0 \\ \Gamma_2: & \dfrac{1}{\mu_1}\frac{\partial A_z}{\partial n} - \dfrac{1}{\mu_2}\dfrac{\partial A_z}{\partial n} = J_s \end{cases}, \tag{1}$$

where: Ω is the calculation region, A_z and J_z are the magnetic vector potential and the source current density in the z-axial component, respectively, J_s is the equivalent current density of permanent magnets, n is the normal direction of permanent magnet boundary, σ is the conductivity, μ is the permeability, Γ_1 is the parallel boundary condition, Γ_2 is the PM boundary condition, μ_1 and μ_2 are the relative permeability, and t is the time.

2.2. Experimental test and data comparison

In order to verify the accuracy of the model, the prototype is tested by an experimental platform. The experimental platform includes a Magtrol dynamometer machine, HIOKI PW6001 power analyzer, industrial condensing unit, DSP data acquisition system and other experimental equipment. The experimental platform of the prototype is shown in Fig. 2. Under different operating conditions, the experimental data of torque, no-load back EMF and current are obtained. The experimental data is compared with the calculated data, as shown in Fig. 3 and Table 2.

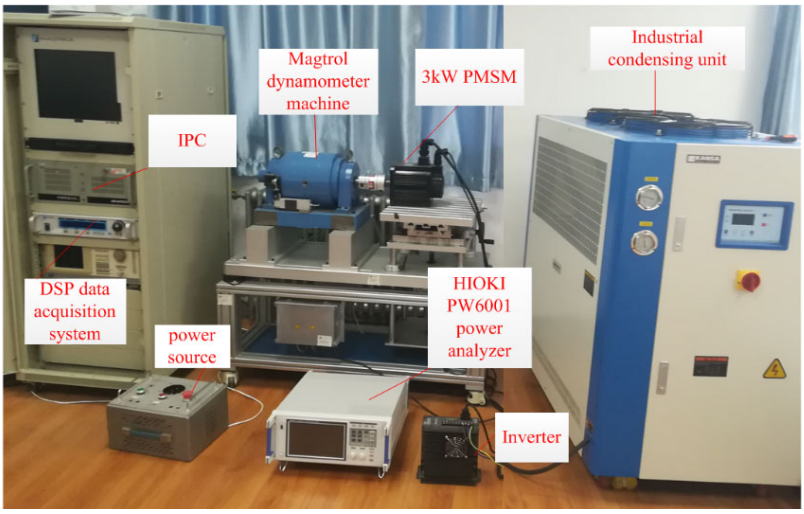

Fig. 2. Prototype test platform

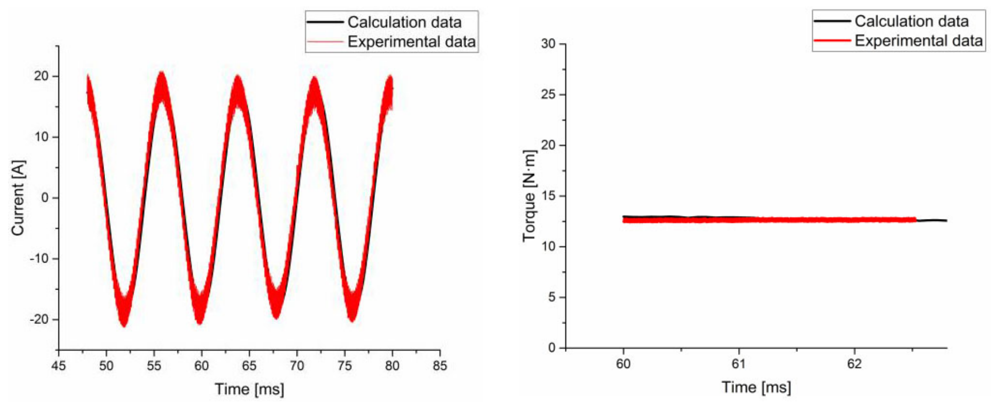

(a) 2 kW load operation

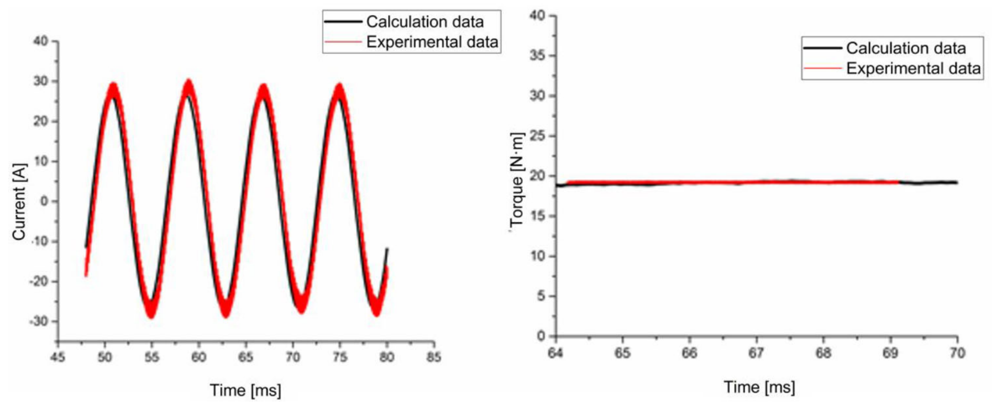

(b) 3 kW load operation

Fig. 3. Comparison between the waveform of simulation and experiment

Table 2. Comparison between experimental data and calculated data

Operation state	Parameter	Experimental data	Calculation data	Variation rate
2 kW	Current (A)	12.77	12.8	0.23%
	Average torque (N·m)	12.71	12.73	0.16%
3 kW	Current (A)	19.4	18.83	2.9%
	Average torque (N·m)	19.11	19	0.57%
No-load back EMF (V)		95.7	94.7	1%

It can be seen from Table 2 that the errors are within 5%. The calculated results are in good agreement with the experimental date under different powers. The accuracy of the model is verified.

3. Performance comparison of PMSM in no-load operation

3.1. The no-load air-gap flux density

In the process of PMSM design, the no-load back EMF is one of important parameters, which need to be accurately calculated. The no-load back EMF can judge the performance

The air-gap flux density is an important parameter in a PMSM, and it has been discussed in depth for a long time. The air-gap flux density affects the size of a magnetic energy product and the power intensity of the PMSM, and directly determines the ability of the PMSM to drive load. Therefore, in the design of the PMSM, it is necessary to ensure the rationality of the air-gap flux density of the PMSM.

In order to compare the differences of the air-gap flux density between the two winding structures, the air-gap magnetic density is extracted, and the harmonic decomposition is carried out based on the Fourier theory. In this paper, the radial air-gap flux density of the two winding structures is extracted by using Equation (2).

$$B = \cos\theta B_x + \sin\theta B_y\,, \tag{2}$$

where: B is the radial flux density; θ is the electrical angle; B_x is the x-axis component with flux density; B_y is the y-axis component with flux density.

The no-load air-gap flux density waveforms of different winding structures and the results of the Fourier harmonic decomposition in one cycle are shown in Fig. 4.

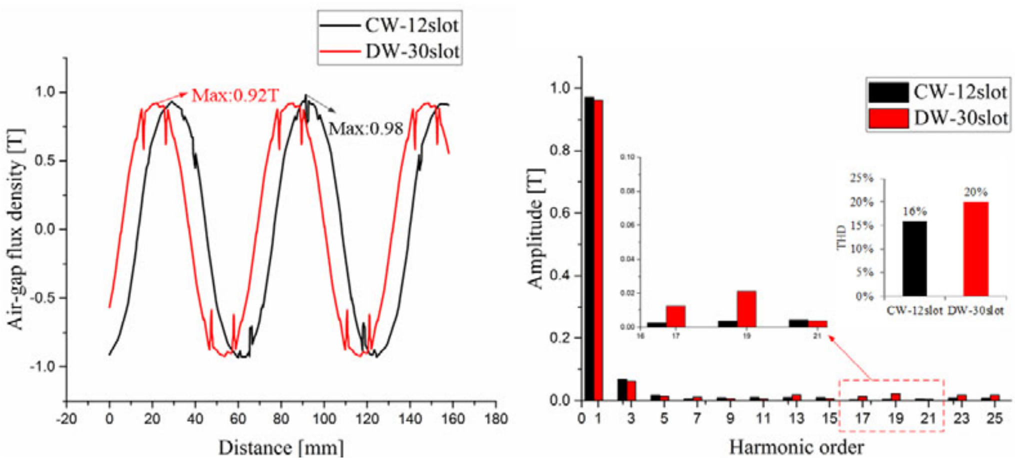

Fig. 4. The waveform and harmonic content of air-gap flux density at no-load

It can be found from Fig. 4 that the maximum air-gap flux density of the CW-12slot is higher than that of the DW-30slot. When the motor is running with no load, the maximum air-gap flux density of CW-12slot is 0.98 T, and the maximum air-gap flux density of DW-30slot is 0.92 T. The difference of air-gap magnetic density is mainly caused by the different winding structure, which leads to the difference of slot size and further leads to the difference of magnetoresistance.

In order to accurately compare the harmonic content of the two winding structures, based on the Fourier decomposition theory, the air-gap flux density of a period is extracted and the harmonic decomposition is carried out.

It is found that the THD of no-load air-gap flux density of the CW-12slot and DW-30slot are 16% and 20%, respectively. The THD of the no-load air-gap flux density of the CW-12slot is 20% lower than that of the DW-30slot.

3.2. The no-load back EMF

The pulsating torque is the harmonic torque which is caused by the interaction between the harmonics of a magnetic field and the stator current. These harmonics are related to the spatial distribution of the winding and the excitation magnetic field produced by permanent magnets. In order to reduce the ripple torque, the no-load back EMF harmonics are minimized as much as possible in the process of motor design [10].

The quality and magnitude of the no-load back EMF depends on the winding factors, the number of turns per phase, fundamental component of magnet flux, synchronous frequency, as shown in (3) [11].

$$\begin{cases} E_0 = \dfrac{2\pi}{\sqrt{2}} \left(k_w N_{ph}\right) \lambda_m f \\ k_w = k_p k_d k_{\text{skew}} \end{cases}, \tag{3}$$

where: K_w is the winding factor; N_{ph} is the number of turns per phase; λ_m is the fundamental component of magnet flux; f is the synchronous frequency; k_p is the pitch factor; k_d is the distribution factor; k_{skew} is the skewing factor.

It can be seen from the above equation that the difference of winding structure will directly cause the difference of winding factor, and then affects the no-load back EMF of the PMSM. The waveforms of the no-load back EMF and harmonic contents of the no-load back EMF are given in Fig. 5.

From the no-load back EMF waveforms of the two winding structures in Fig. 5, it can be seen that the no-load back EMF waveform of the CW-12slot is more sinusoidal, and the no-load EMF

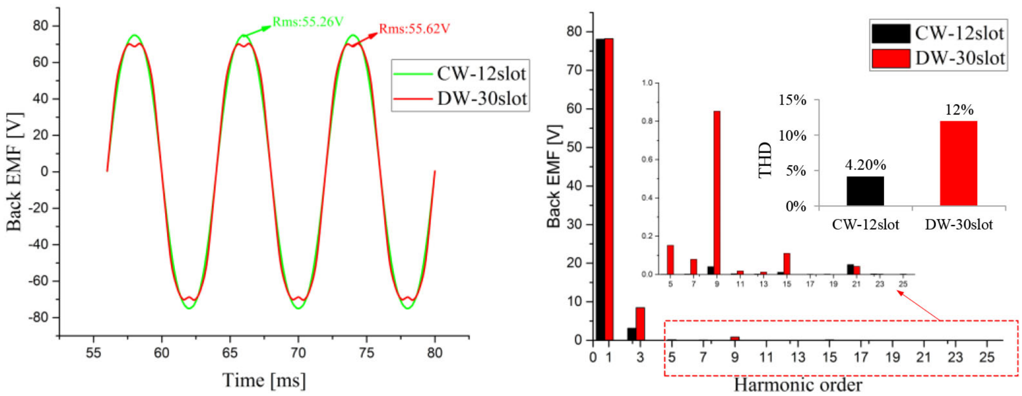

Fig. 5. The waveform and harmonic content of no-load back EMF at no-load

RMS of the CW-12slot is lower than that of the DW-30slot. The RMS of no-load back EMF of the CW-12slot and DW-30slot are 55.26 V and 55.62 V, respectively.

Comparing and analyzing the harmonic spectrum of the two winding structures, it can be found that only the 21th harmonic content is higher than the DW-30slot, and the other harmonic contents are lower than the DW-30slot. The total harmonic contents of the CW-12slot are smaller.

The THD of the no-load back EMF of the CW-12slot and DW-30slot are 4.2% and 12%, respectively, and the THD of the CW-12slot is 65%, which is less than that of the DW-30slot. The harmonic contents of the no-load back EMF of the CW-12slot are much lower than that of the DW-30slot. According to the above analysis, the torque ripple of the CW-12slot should also be far lower than the DW-30slot. The differences of cogging torque between the two winding structures will be compared and analyzed in the next section.

3.3. Cogging torque

Cogging torque is a kind of pulsating torque which can cause vibration and noise of a PMSM. It is known that the cogging torque is greatly influenced by the topology of the PMSM and thus it is possible to minimize the cogging torque by optimizing the design [12, 13]. This section analyses the cogging torque from the energy point of view. The analytical expression shows the key points of reducing the cogging torque. The expression of the cogging torque is shown in Equation (4) [14, 15].

$$\begin{cases} T_{\text{cog}}(\theta) = -\dfrac{L_{ef} B_\sigma^2 N_s N_p}{\pi \mu_0 N_L} \left(R_2^2 - R_1^2\right) \times \\ \qquad \times \sum\limits_{n=1}^{\infty} \dfrac{K_{skn}}{n} \sin\left(n N_L \dfrac{b_0}{2}\right) \sin\left(n N_L \dfrac{\pi \alpha_p}{N_p}\right) \sin\left(n N_L \theta - \dfrac{1}{2} n N_L \alpha_s\right) \\ K_{skn} = \dfrac{\sin\left(\dfrac{1}{2} n N_L \alpha_s\right)}{\dfrac{1}{2} n N_L \alpha_s} \end{cases}, \tag{4}$$

where: L_{ef} is the effective axial length of the PMSM, B_σ is the maximum air gap flux density due to the permanent magnets, N_s is the number of slots, N_p is the pole number, N_L is the lowest common multiple (LCM) of N_s and N_p, μ_0 is the permeability of air, R_1 is the inner radius of the air gap, R_2 is the outer radius of the air gap, b_0 is the slot opening, α_p is the pole-arc to pole-pitch ratio, α_s is the skewing angle and K_{skn} is the skew factor.

The design parameters of influences the cogging torque can be clearly obtained from Equation (5), such as the effective length of the core, the maximum air gap flux density, the pole-arc factor, etc. However, in the process of designing two motors, the consistencies of some parameters are guaranteed to the greatest extent. In addition, the LCM of the two motors is significantly different, and the larger the LCM, the smaller the cogging torque is.

In order to verify the correctness of the above analysis results, the cogging torque of two motors with different winding structures is analyzed based on the FEM. The cogging torque of the two motors with different winding structures is shown in Fig. 6.

It can be seen from Fig. 6 that the maximum cogging torque of the DW-30slot is 330 mN·m, and the maximum cogging torque of the CW-12slot is only 22 mN·m. The cogging torque of the

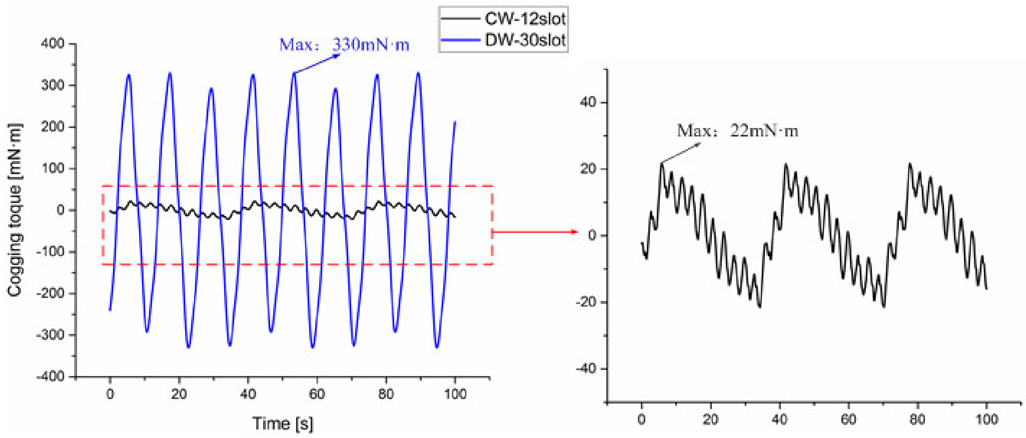

Fig. 6. Comparison of cogging torque for the motor with CW-12slot and DW-30slot

DW-30slot is 15 times higher than that of the CW-12slot, and the cogging torque period of the CW-12slot is shorter. To sum up, the operation stability and the efficiency of the CW-12slot is much higher than that of the DW-30slot. Therefore the cogging torque can be reduced effectively by choosing a proper slot-pole combination.

4. Performance comparison of PMSM in rated power operation

4.1. Torque analysis

Torque ripple of a PMSM refers to a periodic increase or decrease in an output torque as the motor shaft rotates. The torque ripple restricts the application of the PMSM on high-precision occasions, especially in low speed driving situations, and is one of the most important performance indexes of the PMSM. The torque ripple of the PMSM is caused by the cogging torque and ripple torque. The cogging torque has been studied in 3.3, and the influence of the ripple torque on the torque ripple is studied in this section. The distributions of two motor windings are different, and the magnetic circuits of current flow are different when the load is running, and the spatial harmonics of the PMSM have different effects on the current waveform so the ripple torque of the motors will also be different.

In this paper, torque ripple Equation (5) is used to measure the torque ripple [16].

$$T_r = T_{\max} - T_{\min}, \tag{5}$$

where: T_r is the torque ripple, $T_{\max}$ is the maximum torque in a cycle and $T_{\min}$ is the minimum torque in a cycle.

It can be seen from Fig. 7 that the overload capacity of the DW-30slot is 34 N$cdot$m, and the overload capacity of the CW-12slot is 37 N·m, increasing by 9%. The torque ripple of the DW-30slot is 0.7 N·m, and the torque ripple of the CW-12slot is only 0.4 N·m, which is reduced by 43% compared with the torque ripple of the DW-30slot. It can be seen that the CW-12slot is obviously higher than the DW-30slot in overload capacity and operation stability.

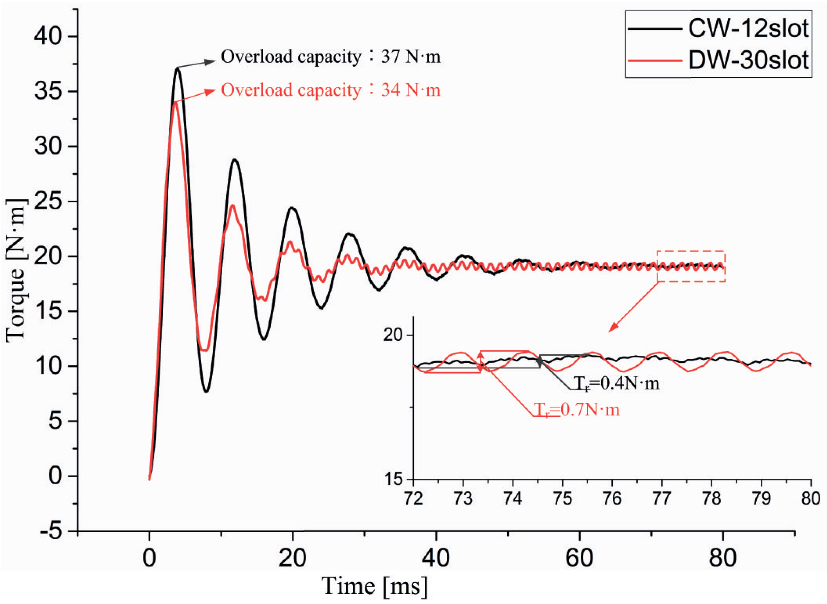

Fig. 7. Torque analysis

4.2. The stator saturation

The stator saturation of the DW-30slot and the CW-12slot is given in Fig. 8. The motor stator presents different degrees of saturation, mainly distributed in the stator teeth. The maximum magnetic flux density of the stator for the CW-12slot and the DW-30slot are 2.12 T and 1.89 T,

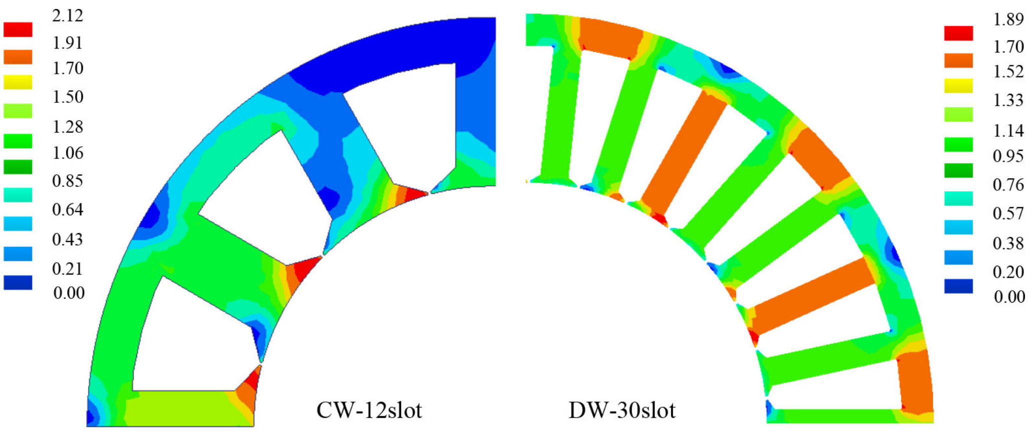

Fig. 8. The stator saturation of distributed winding and centralized winding

respectively. The maximum value of the stator winding magnetic density of the CW-12slot is 12.2% higher than that of the DW-30slot. It can be seen that the CW-12slot can increase the saturation of the stator.

4.3. The analysis of efficiency

The loss is directly related to the efficiency of the PMSM, the bigger the loss, the lower the efficiency. When the winding distribution of the PMSM is different, the current and magnetic field of the PMSM transform greatly, which causes a change in the loss of the motor. Therefore, it is very valuable to study the loss of the PMSM with a different DW and CW.

The loss of the PMSM mainly includes copper loss of the winding, core loss of the stator and rotor, mechanical loss and stray loss. According to the mechanism of core loss, the core loss of the PMSM can be divided into hysteresis loss and eddy current loss, and the eddy current loss can be divided into classical eddy current loss and abnormal loss. The calculation formula of the PMSM core loss is (6) [17].

$$P_{\mathrm{Fe}} = P_h + P_c + P_e = K_h f B^{\alpha} + K_c f^2 B^2 + K_e f^{1.5} B^{1.5}. \tag{6}$$

In the formula, P_{Fe} is the core loss, P_h is the hysteresis loss, P_c is the classical eddy current loss, P_e is the abnormal eddy current loss, K_h K_c K_e represent the loss factor, f is the frequency, B is the flux density. It can be seen from the above formula that the core loss of the PMSM is related to the frequency and the flux density amplitude.

The copper loss is one of the most important heat sources in the motor, and the temperature rise caused by the copper loss is large. Therefore, the accurate calculation of the copper loss is more important. The copper loss can be obtained by Equation (7) [18].

$$P_{\mathrm{Cu}} = 3r_{at} \sum I_i^2, \tag{7}$$

where: I_i contains the fundamental component and the harmonic components of the phase current, and r_{at} represents the phase resistance at operating temperature.

Based on the FEM, the influences of different winding structures on the motor loss are compared and analyzed in this section, and the differences of the motor losses caused by different winding distributions are obtained.

The cause of wind friction loss is complicated, especially the additional loss accounts for a large proportion of the total ventilation loss, so it is difficult to calculate it accurately. The wind friction loss is obtained from the experimental data in Table 3, which can comprehensively consider the theoretical wind friction loss of the motor and the additional losses caused by the processing technology, and the calculation result is very accurate.

Table 3 shows the various losses of the two PMSMs. It can be seen from Table 3 that the copper loss and stator core loss of the DW-30slot are much higher than the CW-12slot, but the eddy current loss is lower than that of the CW-12slot. Compared with the CW-12slot, the copper loss and stator core loss of the PMSM with the DW-30slot increased by 7.2% and 26%, respectively. The eddy current loss of the CW-30slot is less than 9% of the eddy current loss of the DW-12slot. Because the coil of the CW-12slot is placed in the adjacent stator slot, the length of the winding end and the axial length of the PMSM are shortened, thus reducing the copper loss.

Table 3. The loss of CW-12slot and DW-30slot

Winding type	Loss (W)			
	Copper loss	Stator core loss	Eddy current loss	Wind friction loss
CW-12slot	126	35	33	50
DW-30slot	135	44	30	50
Variation rate	7.2%	26%	−9%	0%

Based on the analysis of the various losses of the PMSM with the CW-12slot and DW-30slot, the efficiencies of the two motors are given in Fig. 9. It can be seen from Fig. 9, the efficiencies of the CW-12slot and DW-30slot are 92.5% and 92%, respectively, and the efficiency of the CW-12slot is 0.5% higher than that of the DW-30slot. For the difference of eddy current loss between two winding structures, the mechanism of eddy current loss will be analyzed next.

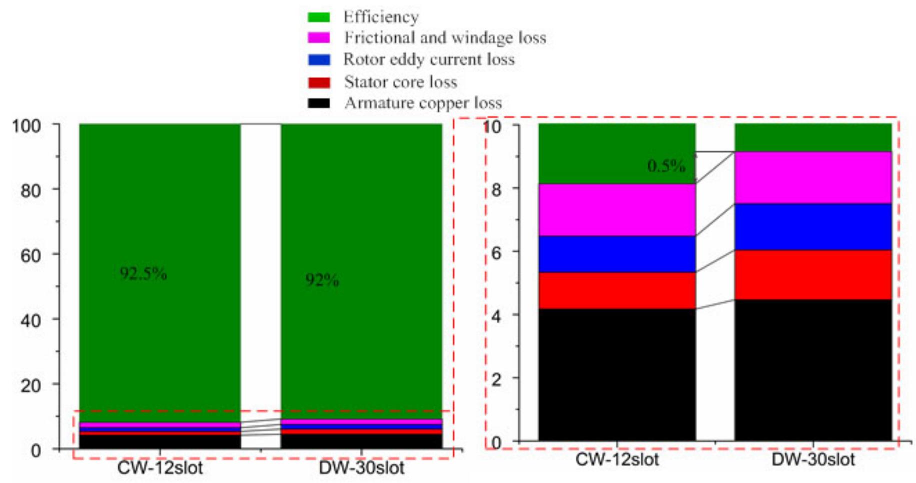

Fig. 9. The efficiency and loss distribution of the two motors

The magnetic field of the PMSM is divided into two parts. The main magnetic field is generated by the permanent magnet. It rotates synchronously with the motor rotor and the main magnetic field cannot form eddy currents on the rotor surface. The other part of the magnetic field is caused by harmonic components, including tooth harmonics, time harmonics, and motor space harmonics, which does not rotate synchronously with the motor rotor. The induced EMF and the eddy current in the conductors are induced by the alternating magnetic flux, and then the eddy current loss is formed. The first part has studied the variation of air-gap flux density at the no-load operation. However, due to the influence of armature reaction, when the rated load is running, the air-gap flux density changes greatly. The difference in the eddy current loss can be analyzed by studying the THD of air-gap flux density at rated load. In addition, according to the calculation formula of eddy current loss, the eddy current loss is also related to the eddy current density.

In order to reveal the influence mechanism of rotor eddy current loss of motor, the eddy current density and the THD of air-gap flux density at rated operation are analyzed by using the finite element method. The eddy current density of the PMSM and the THD of air-gap flux density at rated operation are shown in Fig. 10.

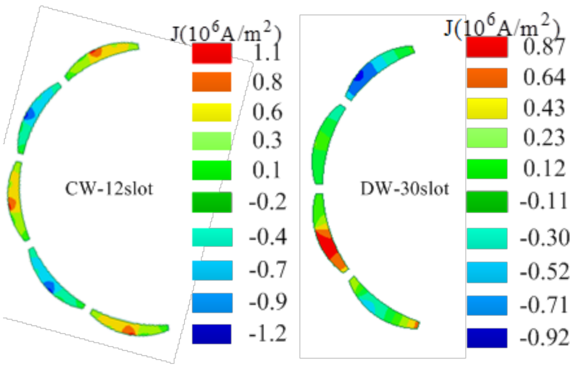

(a) Eddy current density distribution at rated state

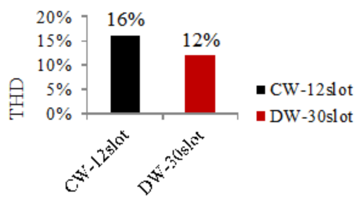

(b) Air gap magnetic density distortion rate at rated state

Fig. 10. The eddy current density and the THD of air-gap flux density at rated operation

During the calculation, the eddy losses in the rotor surface are calculated by (8) in a cycle [19].

$$P_e = \frac{1}{T_e} \int\limits_{T_e} \sum_{i=1}^{k} J_e^2 \Delta_e \sigma_r^{-1} l_t \, \mathrm{d}t, \tag{8}$$

where: P_e is the rotor eddy current losses (in W), J_e is the current density in each element (in A/m^2), Δ_e is the element area (in m^2), l_t is the rotor axial length (in meter), σ_r is the conductivity of the eddy current zone (in S/m), T_e is the time vary period of eddy current density in each element.

The eddy current density of the CW-12slot is much larger than the eddy current density of the DW-30slot. Take the maximum value as an example, the maximum eddy current density values of the CW-12slot and DW-30slot are 1.1×106 A/m^2 and 0.87×106 A/m^2, respectively. Compared with the CW-12slot, the eddy current density of the DW-30slot is reduced by 26%. In addition, it can be seen from the THD of the air-gap flux density at rated load that the THD of the DW-30 slot is 4% lower than that of the CW-12 slot. Low eddy current density and low THD of air-gap flux density are two important factors for low eddy current loss of the DW-30slot.

5. Conclusions

In this paper, a 3 kW 1500 r/min PMSM is taken as an example and based on the FEM, the performance differences between the DW and the CW are analyzed. The following conclusions are obtained:

The design of the CW-12slot significantly improves the operational stability of the PMSM. Compared with the THD of no-load air-gap flux density of the DW-30slot, the THD of the CW-12slot is reduced by 20%, and the THD of the no-load back EMF of the DW-30slot is 3 times that of the DW-12. In addition, the THD of no-load back EMF of the CW-12slot and DW-30slot are 4.2% and 12%, respectively and the THD of the CW-12slot is 65%, which is less than that of the DW-30slot.

The peak cogging torque is inversely proportional to the LCM of the slot number and pole number, and the larger the LCM, the smaller the cogging torque is. The cogging torque can be reduced effectively by choosing a proper slot-pole combination, breaking the general understanding that the more slot number, the smaller cogging torque. The cogging torque of the DW-30slot is 15 times that of the cogging torque of the CW-12slot, and the cogging torque cycle of the CW-12slot is shorter.

At rated operation, the overload capacity of the CW-12slot is higher than the DW-30slot, and the torque ripple of the CW-12slot is significantly lower than the DW-30slot. The overload capacity of the DW-30slot is 34 N·m, and the overload capacity of the CW-12slot is 37 N·m, increasing by 9%.The torque ripple of the DW-30slot is 0.7 N·m, and the torque ripple of the CW-12slot is only 0.4 N·m, which is reduced by 43% compared with the torque ripple of the DW-30slot.

Compared with the DW-30slot, the CW-12 shows higher efficiency. The efficiencies of the CW-12slot and DW-30slot are 92.5% and 92%, respectively, and the difference is 0.5%. The copper loss and stator core loss of the DW-30slot are 7.2% and 26% higher than that of the CW-12slot, respectively, and the eddy current loss is 9% lower than that of the CW-12slot.

The differences of the eddy current density and the harmonic contents of air-gap flux density at rated load are the main factors that cause the differences of eddy current loss between the two winding structures. The eddy current density of the CW-12slot is much larger than the eddy current density of the DW-30slot and the differences of maximum eddy current density between the two winding structures are 26%. The influence by the armature reaction, the air-gap flux density of rated operation is greatly different from air-gap flux density of no-load. The THD of air-gap flux density at rated operation of the CW-12slot is 4% higher than that of the DW-30slot.

Acknowledgements

This work was supported in part by the National Natural Science Foundation of China under Grant 51507156, in part by the University Key Scientific Research Programs of Henan province under Grant 17A470005, in part by the Key R & D and Promotion Projects of Henan Province under Grant 182102310033, in part by the Doctoral Program of Zhengzhou University of Light Industry under Grant 2014BSJJ042, and in part by the Foundation for Key Teacher of Zhengzhou University of Light Industry.

References

[1] Zhu G., Zhu Y., Zhu J., *Double-Circulatory Thermal Analyses of a Water-Cooled Permanent Magnet Motor Based on a Modified Model*, IEEE Transactions on Magnetics, vol. 54, no. 3, pp. 1–4 (2018).

[2] Zhang B., Qu R., Wang J., Chen Y., *Thermal Model of Totally Enclosed Water-Cooled Permanent-Magnet Synchronous Machines for Electric Vehicle Application*, IEEE Transactions on Industry Applications, vol. 51, no. 4, pp. 3020–3029 (2015).

[3] Chevailler S., Feng L., Binder A., *Short-Circuit Faults in Distributed and Concentrated Windings of PM Synchronous Motors*, 2007 European Conference on Power Electronics and Applications, pp. 1–10 (2007), DOI: 10.1109/EPE.2007.4417416.

[4] el-Refaie A.M., Shah M.R., *Comparison of Induction Machine Performance with Distributed and Fractional-Slot Concentrated Windings*, 2008 IEEE Industry Applications Society Annual Meeting, IAS, Edmonton (AB, Canada), pp. 1–8 (2008), DOI: 10.1109/08IAS.2008.30.

[5] Bacher J.P., Muetze A., *Comparison of an Induction Machine with Both Conventionally Distributed and Fractional-Slot Concentrated Stator Windings*, Elektrotechnik Und Informationstechnik, vol. 132, no. 1, pp. 39–45 (2015).

[6] Chong L., Rahman M.F., *Comparison of d- and q-axis Inductances in an IPM Machine with Integral-Slot Distributed and Fractional-Slot Concentrated Windings*, 2008 18th International Conference on Electrical Machines, pp. 1–5 (2008), DOI: 10.1109/ICELMACH.2008.4800107.

[7] Brown I.P., Sizov G.Y., Brown L.E., *Impact of Rotor Design on Interior Permanent-Magnet Machines with Concentrated and Distributed Windings for Signal Injection-Based Sensorless Control and Power Conversion*, IEEE Transactions on Industry Applications, vol. 52, no. 1, pp. 136–144 (2016).

[8] Han J., Li W., Wang L., Zhou X., Zhang X., Li Y., *Calculation and analysis of the surface heat-transfer coefficient and temperature fields on the three-dimensional complex end windings of a large turbogenerator*, IEEE Transactions on Industrial Electronics, vol. 61, no. 10, pp. 5222–5231 (2014).

[9] Li W., Zhang X., Cheng S., Cao J., *Thermal Optimization for a HSPMG Used for Distributed Generation Systems*, IEEE Transactions on Industrial Electronics, vol. 60, no. 2, pp. 474–482 (2013).

[10] Wang A., Jia Y., Soong W.L., *Comparison of Five Topologies for an Interior Permanent-Magnet Machine for a Hybrid Electric Vehicle*, IEEE Transactions on Magnetics, vol. 47, no. 10, pp. 3606–3609 (2011).

[11] Chong L., Dutta R., *Comparison of Concentrated and Distributed Windings in an IPM Machine for Field Weakening Applications*, 20th Australasian Universities Power Engineering Conference, Christchurch, New Zealand, pp. 1–5 (2010).

[12] Choi J.S., Izui K., Nishiwaki S., *Topology Optimization of the Stator for Minimizing Cogging Torque of IPM Motors*, IEEE Transactions on Magnetics, vol. 47, no. 10, pp. 3024–3027 (2011).

[13] Barcaro M., Bianchi N., *Torque Ripple Reduction in Fractional-Slot Interior PM Machines Optimizing the Flux-Barrier Geometries*, 2012 XXth International Conference on Electrical Machines, pp. 1496–1502 (2012), DOI: 10.1109/ICElMach.2012.6350076.

[14] Zhu Z.Q., *Influence of Design Parameters on Cogging Torque in Permanent Magnet Machines*, IEEE Transactions on Energy Conversion, vol. 15, no. 4, pp. 407–412 (2000).

[15] Zhu L., Jiang S.Z., Zhu Z.Q., Chan C.C., *Analytical Methods for Minimizing Cogging Torque in Permanent-Magnet Machines*, IEEE Transactions on Magnetics, vol. 45, no. 4, pp. 2023–2031 (2009).

[16] Kermanipour M.J., Ganji B., *Modification in Geometric Structure of Double-Sided Axial Flux Switched Reluctance Motor for Mitigating Torque Ripple*, Canadian Journal of Electrical and Computer Engineering, vol. 38, no. 4, pp. 318–322 (2015), DOI: 10.1109/CJECE.2015.2465160.

[17] Yang C., Zhang Y., Qiu H., *Influence of Output Voltage Harmonic of Inverter on Loss and Temperature Field of Permanent Magnet Synchronous Motor*, IEEE Transactions on Magnetics, vol. 55, no. 6 (2019), DOI: 10.1109/TMAG.2019.2899468.

[18] Qiu H., Wei Y., Yang C., Fan X., *Influence of Different Frequency Harmonic Generated by Rectifier on High-speed Permanent Magnet Generator*, Journal of Electrical Engineering and Technology, vol. 13, no. 5, pp. 1956–1964 (2018).

[19] Li W.L., Wang J., Kou B.Q., *Loss Calculation and Thermal Simulation Analysis of High-Speed PM Synchronous Generators With Rotor Topology*, 2010 International Conference on Computer Application and System Modeling, pp. V14-612–V14-616 (2010).